UNIVERSIDAD DE CONCEPCIÓN
FACULTAD DE INGENIERÍA
DEPARTAMENTO DE INGENIERÍA ELECTRICA

DEVELOPMENT OF MODULES WITH HYBRID TECHNOLOGY BASED ON InP AND SiGe FOR APPLICATIONS IN THE W BAND (75 - 110 GHz).

POR FELIPE ANDRES VARGAS MILLALONCO

Profesor Guía: Rodrigo Revees,Ph.D.

Profesor Co-Guía: Mikko Varonen,Ph.D.

Tesis presentada a la Facultad de Ingeniería de la Universidad de Concepción para optar al grado académico de doctor en ciencias de la ingeniería con mención en ingeniería eléctrica.

Concepción, Chile
July 25, 2025

Derechos de autor

Abstract

This thesis presents the development and characterization of microwave structures based on Low-Temperature Co-fired Ceramic (LTCC) technology, specifically using the Ferro A6M-E substrate, for applications in millimeter-wave radio astronomy instrumentation. A complete methodology is proposed, encompassing the design, electromagnetic simulation, fabrication, and measurement of microstrip structures, with the aim of extracting key dielectric parameters such as relative permittivity (ϵ_r) and loss tangent (tanδ).

Two sets of ring resonator and transmission line structures were designed and fabricated, and their electromagnetic responses were evaluated under both room temperature (300 K) and cryogenic (20 K) conditions. In a novel extension, the frequency range of measurement spans from 1 to 180 GHz, covering both the W band (75–110 GHz) and the D band (110–170 GHz), in order to assess the dielectric behavior of the LTCC substrate with thin-film copper metallization.

The experimental results demonstrate the dielectric stability of the LTCC A6M-E substrate, even under cryogenic conditions, with minimal variation in relative permittivity values and a moderate increase in loss tangent at low temperatures. These findings align well with simulation data and analytical models, confirming the material's suitability for high-frequency applications in demanding environments.

Ultimately, the results validate the hypothesis that LTCC substrates enable the

implementation of hybrid heterodyne modules in the millimeter-wave domain by integrating Indium Phosphide (InP) and Silicon-Germanium (SiGe) technologies. This hybrid approach supports the development of compact and scalable front-end receivers suitable for multi-pixel detection systems operating in mm-wave bands, with direct impact on next-generation instrumentation for radio astronomy.

Acknowledgements

I would like to begin by expressing my deepest gratitude to God for providing me with he spiritual strength and clarity needed to face each stage of this challenging yet enriching journey. His presence was an anchor in the most uncertain moments. To my parents, Amalia Millalonco and José David Vargas, thank you for your patience, your understanding during times of absence, and your unwavering love throughout all these years. You have been my emotional foundation, always believing in my ability to learn and grow. To my life partner, Tamara Guenul, thank you for being a part of this journey for standing by me with tenderness and care when everything seemed overwhelming. Your constant support has been essential for me to reach this point. To my friends and colleagues, who offered advice, joy, understanding, and sincere companionship throughout a process that would have been far lonelier without you. Every conversation, every shared laugh, every act of empathy meant the world to me. To my thesis advisor, Professor Rodrigo Reeves, thank you for your generous guidance, trust, and patience. Your presence was crucial not only in the academic realm but also personally—your human support made a significant difference in difficult times. And to my co-advisor, Mikko Varonen, I am grateful for your dedicated collaboration and technical insight, which greatly strengthened this work.

Agradecimientos

Quiero comenzar agradeciendo profundamente a Dios, por brindarme la fuerza espiritual y la claridad necesaria para enfrentar cada etapa de este desafiante pero enriquecedor camino. Su presencia fue un ancla en los momentos más inciertos. A mis padres, Amalia Millalonco y José David Vargas, gracias por su paciencia, su comprensión en los momentos de ausencia y su amor constante durante todos estos años. Ustedes han sido mi sustento emocional, confiando siempre en mi capacidad para aprender y crecer. A mi compañera de vida, Tamara Guenul, gracias por ser parte de este proceso, por estar conmigo en esta travesía con ternura y cuidado que me sostuvo cuando todo parecía demasiado. Tu apoyo constante ha sido esencial para que pudiera llegar hasta aquí. A mis amigos y colegas, que aportaron con consejos, alegría, comprensión y compañía sincera en un proceso que, sin ellos, habría sido mucho más solitario. Cada conversación, cada risa compartida, cada gesto de empatía tuvo un valor inmenso. A mi director de tesis, el profesor Rodrigo Reeves, gracias por su guía generosa, su confianza y su paciencia. Su presencia fue clave no solo en el aspecto académico, sino también en lo personal, en momentos de dificultad, su apoyo humano marcó una gran diferencia. Y a mi co-director, Mikko Varonen, le agradezco por su colaboración comprometida y visión técnica que fortaleció este trabajo. Este viaje ha sido mucho más que una investigación. Ha sido un proceso de transformación personal, y no habría sido posible sin todos ustedes.

List of Figures

List of Tables

Contents

1 Introduction

The field of radio-astronomical instrumentation entails the development of new receivers designed to explore a wide range of the astronomical spectrum. These receivers are used to identify various phenomena, including molecular transitions in star-forming regions, observations of the cosmic microwave background (CMB), and the detection of objects that emit energy across different frequency bands [2, 3]. To conduct these investigations, highly complex and technologically advanced instruments, such as radiometers [4] and spectrometers [5], are employed to observe the universe in radio frequencies (RF).

Scientific progress in astronomical observations, atmospheric remote sensing studies, and satellite and wireless communications, depend mainly on developing new receivers, particularly in the design of new front-end modules with improved characteristics. These modules should demonstrate high levels of integration in single package, requiring modern component design, and cutting-edge manufacturing techniques such as integrated multi-chip modules (MCM) or System-on-Package (SOP). Indeed, manufacturing these modules involves the integration of different circuits and devices, such as band-pass filters, oscillators, transmission lines, and antennas into substrates with useful and special mechanical and electrical requirements set for optimum operation in the relevant thermal environment [6].

Currently, Low-Temperature Co-fired Ceramic (LTCC) is one of the most promising multichip packaging technologies regarding substrates. This technology is based on a multilayer manufacturing process [7, 8], and its use for packaging circuits in RF, microwave, and millimeter wave frequencies has demonstrated high versatility for the production of modules with high levels of integration and performance. Moreover, LTCC has become a good solution for solving technical problems that require low-temperature operation [9, 10, 11].

Nevertheless, the design of high-frequency systems requires materials with low dielectric loss at microwave and millimeter-wave frequencies, and suitable thermomechanical properties for the operational environment [6]. Therefore, it is essential to understand the electrical properties of the LTCC materials that are currently used for fabricating multichip modules [12, 13], and that will be used in the future in packaging purposes.

Additionally, the modules used in receiver front-ends installed in radio-telescopes are typically operated at cryogenic temperature to reduce the noise temperature produced by the active electronic components. Therefore, understanding and characterizing LTCC materials at W-band for all possible environmental conditions, particularly at cryogenic temperatures, is critical for the correct operation of the integrated modules, as this information can be relevant to determine module noise parameters and to produce more optimized designs [14].

The electrical properties of the LTCC material have been documented for different frequency ranges at room temperature. However, information regarding the dielectric characteristics of LTCC material at cryogenic temperatures is scarce and needs to be explored, particularly in it use at millimeter-wave frequencies.

This work focuses on characterizing the dielectric properties of permittivity and signal loss of LTCC Ferro A6M-E material through measurements carried out under vacuum conditions at room (300 K) and cryogenic (20 K) temperatures. This work provides relevant information required for designing new multichip modules for the development of astronomical instruments, and other industrial applications that face similar operating conditions and requirements, such as space applications.

1.1 Motivation

This research is a systematic exploration of new technology for the development of millimeter wave receivers in the W band (75 - 110 GHz). The proposed methodology involves the hybrid integration of devices based on Indium Phosphide (InP) and Silicon Germanium (SiGe), and the development of housings for the front-end elements of the receiver. The main objective is to reduce their size for integration in multi-pixel cameras, where one of the key requirements for the development of such arrays is low power consumption, which can be addressed through the use of MMIC LNAs based on SiGe technology [15, 16]. Figure 1.1 provides a detailed block diagram with the different internal units of a heterodyne receiver module in the W band, which are key components in the context of astronomical observation instruments, the specific area of focus for this thesis work.

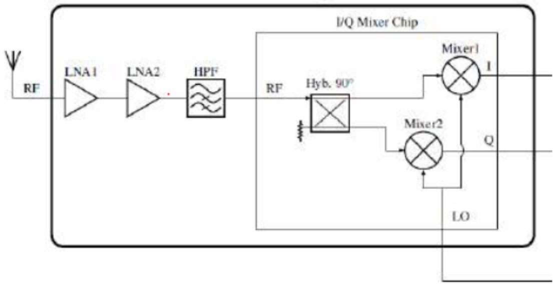

Figure 1.1: General block diagram of a millimeter-wave front-end receiver illustrating the internal components of a heterodyne receiver module, including signal amplification, frequency conversion, and filtering stages.

1.2 Hypothesis

The use of Low-Temperature Co-fired Ceramic (LTCC) materials as substrate platforms provides the necessary electromagnetic, thermal, and mechanical properties for radio-frequency applications. On one hand, LTCC enables operation under cryogenic conditions in the W band (75–110 GHz); on the other hand, it supports the advancement of LTCC technology toward the D band (110–170 GHz) through the use of thin-film techniques. These characteristics make LTCC a suitable candidate for enabling the hybrid integration of Indium Phosphide (InP) and Silicon-Germanium (SiGe) technologies in high-frequency front-end modules. Therefore, it is hypothesized that hybrid W-band heterodyne spectral conversion modules, comprising low-noise amplifiers and mixers, can be effectively implemented using LTCC substrates for radio astronomy applications.

1.3 Objetives

1.3.1 Main objetive

Develop and implement a methodology for the design, simulation, fabrication, and characterization of microstrip structures on LTCC substrates for radioastronomical instrumentation, focusing on the extraction of permittivity, loss tangent and total loss parameters in the W-band under both room temperature and cryogenic conditions.

1.3.2 Specific objetives

- Investigate various interconnection and transition techniques that enable the electromagnetic characterization of substrates used in radioastronomical instrumentation, considering the operational requirements in the W-band.
- Design microstrip structures using LTCC substrates, tailored to the electromagnetic and operational demands specific to the W-band.
- Simulate the designed microstrip structures in an electromagnetic environment using specialized simulation tools to evaluate their performance and optimize the design prior to fabrication.
- Fabricate the microstrip structures on LTCC substrates, adhering to the operational requirements for the W-band and complying with applicable manufacturing standards.
- Characterize the fabricated structures at both room temperature and cryogenic conditions to obtain the response parameters, specifically the S-parameters, within the W-band frequency range.
- Evaluate the measured response of the structures under test to extract the permittivity and loss tangent parameters of the LTCC substrate used.

2 Microwave technologies - technical aspects

2.1 Low Temperature Cofired Ceramics (LTCC)

Low-Temperature Co-fired Ceramic (LTCC) technology has emerged as a versatile and effective solution for the miniaturization of high-frequency components in wireless and communication systems. It allows the integration of multiple passive devices such as bandpass filters, oscillators, waveguides, and antennas within a compact multilayer ceramic structure [17]. This miniaturization is driven by the material's favorable electrical characteristics, including its relative permittivity, where higher values support component size reduction, while lower values enable faster signal propagation, and its low dielectric losses. Moreover, LTCC offers good thermal stability, which is essential for ensuring consistent performance in high-frequency applications, including radioastronomy and satellite communications [18].

One of the advantages of LTCC over traditional packaging technologies like High-Temperature Co-fired Ceramic (HTCC) lies in its firing process. LTCC materials are sintered at temperatures below 1000 °C, which makes it possible to co-fire the ceramic with highly conductive metals such as silver, copper, or gold [17, 19]. This is in contrast to HTCC, which requires refractory metals like tungsten or molybdenum due to its higher sintering temperatures. The compatibility with low-resistance metals improves electrical performance and opens the door to fabricating low-loss transmission lines and embedded components. Additionally, LTCC substrates support the integration of passive elements (resistors, capacitors, inductors) within the ceramic layers, contributing to further size reduction and improved reliability in densely packed RF modules [20].

Besides its excellent electrical properties, LTCC offers mechanical benefits including rigidity, environmental resilience, and hermetic sealing—characteristics that are critical for high-reliability systems operating in extreme environments such as space, defense, and cryogenic applications. These features have led to its growing adoption in millimeter-wave technologies, where precise dimensional and dielectric control are necessary for circuit performance. Given its multifaceted advantages, understanding the fabrication process of LTCC substrates becomes essential for enabling their use in high-frequency and hybrid integration platforms like those explored in this thesis.

The fabrication process of LTCC substrates involves a sequential layering and processing of individual glass-ceramic tapes, commonly referred to as ”green sheets.” Each layer is prepared separately to form the final multilayer structure. The process begins with the creation of via holes using mechanical punching, which serve as vertical electrical or thermal interconnections between layers. These vias are then filled with high-conductivity metal pastes—typically silver (Ag) or gold (Au), and subsequently dried to remove solvents. Following this, conductor patterns and passive elements are screen-printed or photo-imaged onto the tape surfaces. To accommodate embedded components or cavities, selected areas of the sheets are mechanically opened before the layers are precisely aligned using registration holes. The stacked sheets are then laminated under isostatic pressure, often with silicone inserts to preserve cavity shapes. Finally, the entire multilayer assembly is co-fired at temperatures typically ranging from 850 to 900 °C, allowing ceramic sintering and metal coalescence. The resulting panel, which may contain multiple circuits, is then diced into individual modules [20].

Summary of the LTCC Fabrication Process

The entire process is summarized in Figure 2.1, which illustrates the main steps of LTCC substrate manufacturing [17, 20].

- Via Hole Drilling: Holes are created in the green ceramic sheets using mechanical punching techniques.
- Via Metallization: The holes are filled with conductive paste (Ag or Au) via stencil printing.
- Drying: Solvents in the conductive paste are evaporated through thermal drying.
- Conductor Pattern Printing: Metal traces and passive elements are printed onto each individual layer using screen-printing or photoimaging techniques.
- Cavity Formation: Cavities are punched in designated layers to allow for embedded components.
- Layer Alignment and Lamination: The layers are stacked and aligned using registration holes, then laminated under isostatic pressure.
- Sintering or Co-firing: The laminated structure is co-fired at 850–900°C to bond the ceramic layers and metallization.

- Circuit Separation: The fired panel, which may contain multiple circuits, is diced into individual modules.

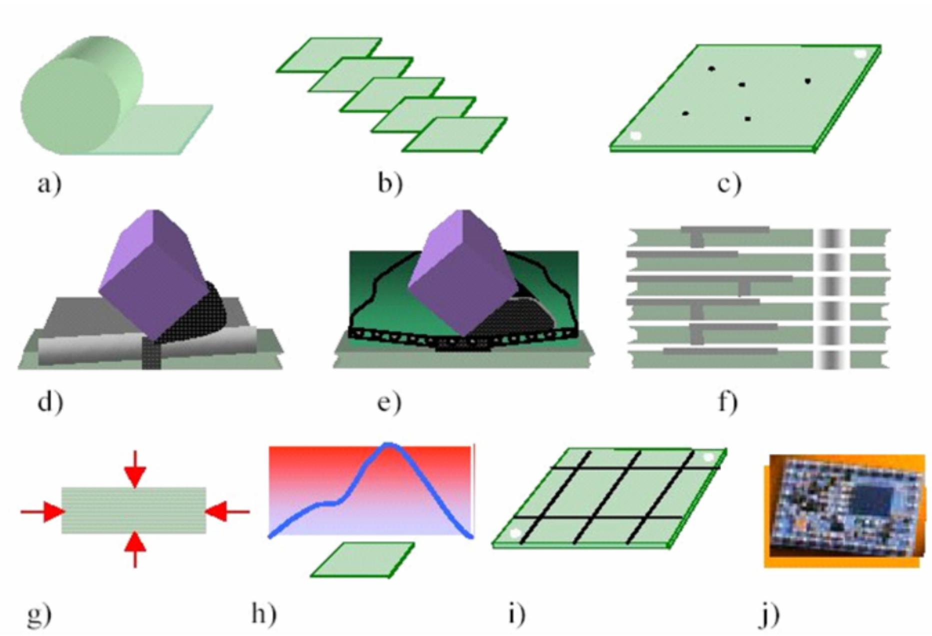

Figure 2.1: The LTCC process: a) glass/ceramic LTCC tape material, b) tape blanking, c) via punching, d) via metallization, e) conductor printing (or photoimaging), f) layer alignment and stacking, g) lamination, h) sintering, i) dicing of fired panel, j) component and die attach.

2.2 Properties of Materials Used in Radio Astronomy in mm-Wave

The dielectric permittivity (ε), tangential losses ($\tan\delta$) and total loss, are important parameters in the selection of materials for radio astronomy applications in n mm-waves. Permittivity determines the propagation of electromagnetic waves through the material, while tangential losses affect attenuation and the efficiency of high-frequency devices.

2.2.1 Dielectric Permittivity

The complex dielectric permittivity is expressed as:

$$\varepsilon^* = \varepsilon' - j\varepsilon'' \tag{2.1}$$

where ε' is the real part, representing the capacity to store electrical energy in the material, and ε'' is the imaginary part, associated with dielectric losses. At W-band frequencies, the materials used must maintain stable permittivity to avoid impedance variations and minimize signal dispersion.

In radio astronomy, materials with low permittivity are employed to reduce wave reflection and improve compatibility with antennas and waveguides. Commonly used materials include quartz (SiO2), polytetrafluoroethylene (PTFE), and low-permittivity ceramics such as Al2O3, which exhibit ε' values ranging from 3 to 10, depending on composition and operating frequency [21].

2.2.2 Tangential Losses and Their Impact

Tangential losses, defined as:

$$\tan\delta = \frac{\varepsilon''}{\varepsilon'} \tag{2.2}$$

indicate the fraction of electromagnetic energy converted into heat due to dielectric dissipation. At W-band frequencies, losses can increase due to dispersion effects and material polarization, affecting the sensitivity of receivers and the efficiency of passive components.

Materials such as PTFE and Rogers RT/duroid 5880 exhibit tangential losses below 0.001 at 10 GHz, but these may slightly increase in the W band due to molecular interactions. On the other hand, materials such as AlN and Al2O3 offer low loss ($\tan\delta < 0.0005$) and high thermal stability, making them ideal for high-frequency circuits in radio astronomy [22].

2.2.3 Total attenuation

In a microstrip transmission line, three types of losses are typically present: conductor loss (α_c), dielectric loss (α_d), and radiation loss (α_r). The total attenuation of the structure (α_{tot}) is the sum of these three components, as shown in the following equation [23]:

$$\alpha_{tot} = \alpha_c + \alpha_d + \alpha_r \tag{2.3}$$

It should be noted that α_d increases linearly with frequency, while α_c increases proportionally to the square root of frequency [24].

Therefore, it is essential to consider each of these loss mechanisms when designing and analyzing high-frequency transmission lines. The relative contribution of each term in α_{tot} depends on the materials used, the geometry of the structure, and the operating frequency range. In particular, radiation losses (α_r) become more significant at higher frequencies or in poorly confined configurations, whereas α_c and α_d dominate in intermediate frequency ranges and are highly dependent on the conductor and dielectric properties, respectively. Accurate characterization of these losses is key to optimizing the electromagnetic performance of the system.

2.2.4 Considerations for Radio Astronomy Applications

In radio astronomy applications, material selection depends not only on ε' and $\tan\delta$ but also on factors such as thermal stability, coefficient of thermal expansion (CTE), and compatibility with manufacturing technologies such as thin film and LTCC. Additionally, cryogenic temperatures in some radio astronomy systems reduce dielectric losses, improving circuit performance [25].

In conclusion, permittivity and tangential losses in the W band directly influence the design and operation of radio astronomy systems. Selecting materials with low ε' and $\tan\delta$ ensures minimal losses and stability of devices in this frequency range.

2.3 Semiconductor Technologies for mm-Wave Applications: SiGe and InP

Silicon-Germanium (SiGe) technology has become a key enabler in the development of circuits operating at millimeter-wave (mmWave) frequencies. It offers an effective balance between performance, cost, and integration, particularly when compared to more expensive III-V semiconductor technologies. SiGe heterojunction bipolar transistors (HBTs), fabricated using BiCMOS processes, allow for the co-integration of high-speed analog/RF circuits with digital and mixed-signal logic on a single die. This integration capability makes SiGe a preferred choice for a wide range of mmWave applications, including wireless communications, radar systems, imaging, and scientific instrumentation.

The evolution of SiGe over the last few decades has been marked by consistent improvements in frequency performance and device scalability. Early SiGe HBTs achieved cutoff frequencies (f_t) around 50 GHz, suitable for lower microwave applications. In subsequent generations, process enhancements pushed f_t and maximum oscillation frequencies (f_{max}) well beyond 200 GHz. Today, advanced SiGe platforms routinely reach or exceed 300 GHz in both parameters, making them competitive with III-V technologies in many high-frequency domains. This advancement has allowed SiGe to support increasingly demanding applications, including high-data-rate transceivers, compact radars, and broadband sensors.

In addition to high-frequency capability, SiGe offers key benefits such as low noise performance, energy efficiency, and high integration density. Its compatibility with standard CMOS fabrication enables the monolithic implementation of complete mmWave systems, significantly reducing package size and cost. SiGe-based devices are now commonly found in low-noise amplifiers (LNAs), power amplifiers (PAs), frequency multipliers, mixers, and highly integrated beamforming circuits. These characteristics make it particularly attractive for both commercial and scientific use cases, especially where system complexity, power efficiency, and form factor are critical constraints.

Alongside SiGe, Indium Phosphide (InP) technology represents a high-performance alternative for mm-Wave and sub-terahertz applications where ultimate signal fidelity, noise performance, and power output are required. InP is a III-V compound semiconductor with superior electron mobility and saturation velocity compared to silicon-based technologies. Devices fabricated in InP—particularly high-electron-mobility transistors (HEMTs) and double heterojunction bipolar transistors (DHBTs)—exhibit exceptional characteristics such as low noise figures (often below 1 dB at mmWave frequencies), high gain, and ultra-high cutoff frequencies that can exceed 500 GHz.

InP's advantages make it the technology of choice for applications demanding extremely low noise, high linearity, and wide bandwidth. It is widely used in scientific instrumentation, deep-space communication, high-resolution radar, and radio astronomy. For example, cryogenic low-noise amplifiers based on InP HEMTs are employed in sensitive receivers operating at sub-Kelvin temperatures, where every decibel of noise savings is critical. Moreover, InP supports power amplifiers with high efficiency and output power at mmWave frequencies, though with trade-offs in terms of integration and fabrication cost.

When comparing both technologies, the trade-off becomes clear. While InP offers unmatched performance in high-end scenarios, SiGe provides a more cost-effective, CMOS-compatible, and integrable solution suitable for large-scale deployment. Table 2.1 summarizes key performance differences between SiGe HBTs and InP HEMTs:

Table 2.1: Comparison between SiGe HBTs and InP HEMTs for mmWave Applications

Parameter	**SiGe HBTs**	**InP HEMTs**
f_t (GHz)	250–350	300–500+
Noise Figure (dB)	2–3	< 1.5
Integration	High (CMOS-compatible)	Low
Cost	Low	High

Looking forward, SiGe and InP are expected to coexist as complementary technologies. SiGe will continue to dominate applications requiring high integration and moderate performance at low cost, while InP will remain essential for the most demanding mmWave and THz systems. In future hybrid platforms, both technologies may be co-packaged using advanced substrates and interconnection strategies, leveraging their respective strengths to meet the rigorous demands of next-generation high-frequency systems.

Finally, transmission lines and resonator structures, particularly ring resonators, provide effective methods for characterizing material properties at mmWave and beyond. Their continued development will enhance the precision of dielectric measurements in future applications.

3 mm-Wave specific technologies for radio-astronomy

In the context of radio astronomy, millimeter-wave (mm-wave) receivers demand extremely low noise, high gain, and precise signal integrity across wide frequency bands. Achieving these characteristics requires advanced circuit technologies capable of operating efficiently in the 30–300 GHz range, where electromagnetic losses, component scaling, and material limitations become critical. Among the most effective approaches for meeting these challenges is the use of hybrid integration, which combines different semiconductor platforms to optimize performance across multiple dimensions—noise, gain, power efficiency, and system integration.

Hybrid technology involves the co-integration of high-performance semiconductors such as Indium Phosphide (InP) and Silicon-Germanium (SiGe) within a single front-end module. Each material contributes distinct advantages that complement one another: InP offers exceptional performance in noise and frequency response, while SiGe excels in integration, cost-effectiveness an low power consumption. This combination allows the design of receiver architectures that can meet the stringent sensitivity and resolution requirements of modern radio astronomical instrumentation.

Indium Phosphide (InP) is a III-V compound semiconductor renowned for its superior electron mobility and frequency characteristics. These properties enable InP-based devices—such as High Electron Mobility Transistors (HEMTs) and Heterojunction Bipolar Transistors (HBTs)—to operate well into the sub-terahertz range with minimal noise and high power density. In millimeter-wave circuits, InP transistors commonly achieve cutoff frequencies (f_t) greater than 300 GHz and maximum oscillation frequencies (f_{max}) beyond 1 THz [26]. This high-frequency capability is complemented by excellent low-noise characteristics, with typical noise figures below 1 dB at mm-wave frequencies, making InP an ideal technology for cryogenically cooled low-noise amplifiers (LNAs) used in radio astronomy [27].

Silicon-Germanium (SiGe), on the other hand, offers a CMOS-compatible alternative that balances performance with integration capability and cost efficiency. SiGe technology, typically developed through BiCMOS platforms, enables the monolithic integration of high-speed analog/RF components alongside digital and mixed-signal blocks on the same die. Although it does not reach the ultra-low-noise or ultra-high-frequency performance of InP, modern SiGe processes achieve f_t and f_{max} values in of 300 GHz and 500 GHz, respectively, making them suitable for a wide range of mm-wave applications [28]. SiGe HBTs exhibit low noise figures in the range of 2–5 dB for 2.0 – 30 GHz [29], 70-170 GHz [30], and provide moderate power gain, which is often sufficient for intermediate amplification and signal processing stages. This is particularly valuable in cryogenic applications, where reduced thermal noise and environmental stability help compensate for slight performance differences with InP. Furthermore, SiGe's cost-effective fabrication, high integration density and low power consumption make it ideal for large-scale receiver arrays, focal plane assemblies, and digital beamforming architectures.

The complementary nature of these two technologies has led to the growing adoption of hybrid mm-wave modules in scientific instrumentation. In a typical hybrid configuration, InP components are used in the initial stages of the receiver chain, where noise performance is critical, while SiGe is deployed for functions such as frequency conversion, gain control, or backend signal processing. This approach enables engineers to harness the strengths of both platforms, resulting in highly integrated, compact, thermally efficient and low-power consumption receivers optimized for the demanding requirements of radio astronomical observations. By leveraging hybrid integration, it becomes possible to scale high-performance front-end modules without compromising sensitivity, integration, or thermal performance—crucial factors for next-generation millimeter-wave telescopes and spaceborne observatories.

4 Material Characterization Methodology

This chapter describes the process followed for the electromagnetic characterization of the LTCC (Low-Temperature Co-fired Ceramic) substrate Ferro A6M-E, which is used as the base material for the design and integration of millimeter-wave circuits. Accurate characterization of the dielectric parameters, such as relative permittivity (ϵ_r), loss tangent ($tan\ \delta$) and total loss, is essential for the reliable design of microwave structures, particularly in high-frequency applications such as radio astronomy systems.

The objective of this chapter is to present in detail the experimental methodology used to extract these parameters under realistic operating conditions, both at room temperature and under cryogenic environments. The characterization was performed using custom-designed microstrip transmission line and microstrip ring resonator structures.

4.1 Design and fabrication of first set structures for the characterization of LTCC material

This section describes the design details of the structures developed for the electrical characterization of the LTCC material. The structure stack consists of three 92 μm high LTCC substrate layers, the distance between metals is 82 μm of height (h), and a gold conductive layer with a thickness (t) of 8 μm. The stack of these layers is shown in Fig. 4.1. The bottom two layers are included to provide mechanical robustness, and therefore, multiple vias were placed between the two bottom layers to provide a homogeneous ground connection at the ground plane of the top substrate layer. The top substrate layer is designed for routing RF signals in microstrip mode. The electrical properties of the stack are extracted using the Microstrip Resonant Ring (MRR) method.

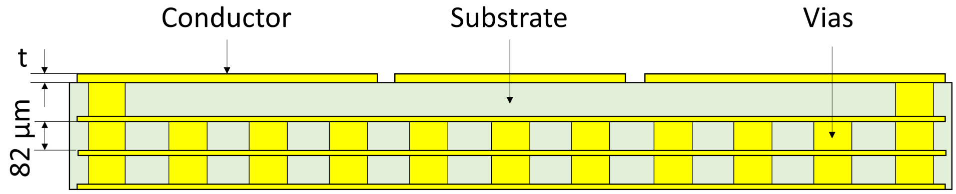

Figure 4.1: Stack up of the LTCC Microstrip Resonant Ring (MRR) structure [1].

4.1.1 Microstrip ring resonator (MRR)

The MRR method is usually used for the characterization of materials since it allows extracting their properties at multiple frequency values with a single measurement [31]. The ring structure produces electromagnetic resonances at specific frequencies set by the mechanical dimensions of the structure, and the electrical parameters of the substrate. By numerically analyzing the forward transmission scattering parameter S_{21} obtained from the structure, the MRR method extracts the electrical parameters of the material. The central frequency of the produced resonances depends on the relative permittivity of the material, while the quality factor parameter of the resonance is used to calculate its loss tangent. For the design of the MRR, the following equation is used [9]:

$$f_n = \frac{nc}{2\pi r_m \sqrt{\varepsilon_{eff}}} \qquad\qquad for\ n = 1, 2, 3... \tag{4.1}$$

Where f_n corresponds to the nth resonance, r_m is the mean radius of the ring, c is the speed of light, and ε_{eff} is the effective dielectric constant. In our design, a single resonance frequency peak ($n = 1$) was selected to calculate the mean radius of the ring. Fig. 4.2 shows the top view of the general MRR layout used, where W is the width of the microstrip signal trace, and S is the length of the separation, or gap, between the ring and the feed line. The MRR geometry is calculated from the equation (4.2), based on the methodology proposed in [32]. In this method, the calculate of the radius r_m, requires first an estimate of ε_{eff} using the following approach,

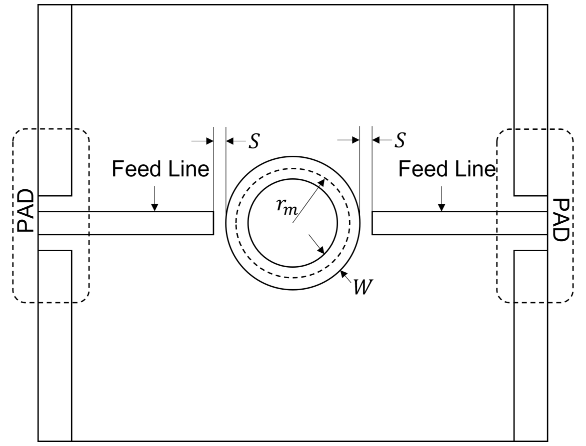

Figure 4.2: General scheme of the adopted and implemented microstrip ring resonator [1].

$$\varepsilon_{eff} = \varepsilon_r - \frac{\varepsilon_r(f) - \varepsilon_{eff}(0)}{1 + P(f)} \tag{4.2}$$

where,

$$P(f) = P_1\, P_2\, \left[(0.18844 + P_3\, P_4)\; 10\, f\, h\right]^{1.5763} \tag{4.3}$$

$$\begin{gathered} P_1 = 0.27488 + \left[0.6315 + \frac{0.525}{(1 + 0.157\, f\, h)^{20}}\right] \\ u - 0.065683\; exp(-8.7513\, u) \end{gathered} \tag{4.4}$$

$$P_2 = 0.33622\; \{1 - exp\; [-0.03442\, \varepsilon_r\, (f)]\} \tag{4.5}$$

$$P_3 = 0.0363\; exp\,(-4.6\, u) \left\{1 - exp\left[-\left(\frac{f\, h}{3.87}\right)^{4.97}\right]\right\} \tag{4.6}$$

$$P_4 = 1 + 2.751 \left\{1 - exp\; \left[-\left(\frac{\varepsilon_r}{15.916}\right)^{8}\right]\right\} \tag{4.7}$$

Where f is the frequency, ε_r is the relative dielectric constant, and u represents the microstrip width-to-height ratio W/h, which is derived from the microstrip characteristic impedance. The value of parameter u is chosen to achieve a characteristic impedance of $Z_0 = 50\ \Omega$, and to calculate the width W of the microstrip. Additionally, the characteristic impedance is calculated using the following approximation, where $\eta_0 = 120\pi$, the free space impedance:

$$Z_0 = \frac{\eta_0}{2\sqrt{2}\,\pi\sqrt{\varepsilon_r+1}} \, ln\left[1+\frac{4}{u}\left(\frac{14+\frac{8}{\varepsilon_r}}{11}\right)+A\right] \tag{4.8}$$

$$A = \sqrt{\left(\frac{14+\frac{8}{\varepsilon_r}}{11}\right)^2\left(\frac{4}{u}\right)^2+\left(\frac{\left(1+\frac{1}{\varepsilon_r}\right)}{2}\right)\pi^2} \tag{4.9}$$

Additionally, to obtain different resonant frequencies in the desired spectral band (75-110 GHz), three rings with different radii were designed with fundamental frequencies centered at 80, 90, and 100 GHz, as shown in Fig. 4.3. The physical dimensions of the fabricated circuit were extracted with high resolution microscopy, and a summary of the measured dimensions is shown in Table 4.1.

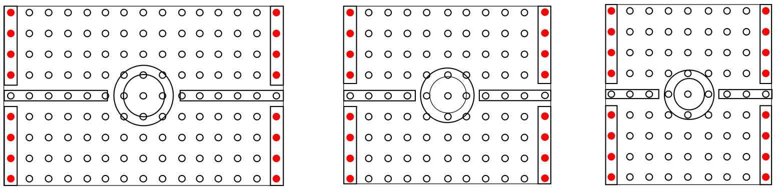

Figure 4.3: Designed MRR structures. From left to right, 80, 90, and 100 GHz resonant structures, respectively. The location of vias is indicated with small circles. The red circle vias connect the pads with the RF ground; all other circles are vias used to connect the two bottom layers [1].

To be able to perform on-wafer S-parameter measurements using ground- signal-ground (GSG) RF probes and properly route the test RF signal through the structure, probe pads (PAD) in GSG configuration and microstrip feed lines were added to both sides of the MRR structures. To ensure a well-defined ground return current path for the RF on-wafer measurements, we have integrated pad-to-ground VIAs within the ground pads to establish a good ground connection between the RF test

Table 4.1: Measured dimensions of the manufactured ring. Values in the design and manufacturing columns are in μm [1].

MRR structure	Parameter	Design	Manufactured
80 GHz	r_m	283	279
	W	108	102
90 GHz	r_m	256	255
	W	106	100
100 GHz	r_m	223	222
	W	105	100
All	S	50	64

probes and the microstrip ground plane.

4.1.2 Fabrication

In this work, twelve microstrip resonator rings were fabricated using Ferro A6M - E LTCC (Low-Temperature Co-Fired Ceramic), as shown in Fig. 4.4. These rings were arranged in a matrix format, with each column representing resonators designed for frequencies of 80, 90, and 100 GHz, respectively.

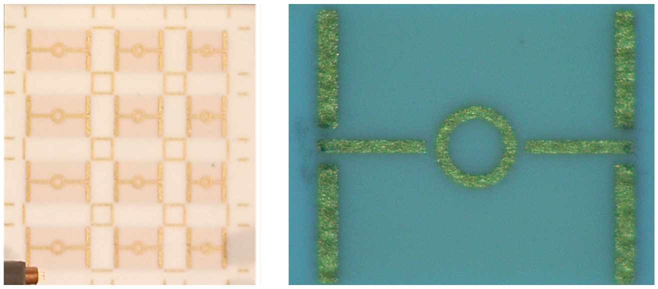

Figure 4.4: Left: LTCC substrate with rings for the three chosen frequencies. The arrangement contains four MRR structures per frequency. Right: magnified photograph of one of the fabricated rings [1].

For the evaluation of the transmission performance of the LTCC substrate, a coplanar waveguide (CPW) transmission line with a length of 1200μ m was fabricated, as shown in Fig 4.5.

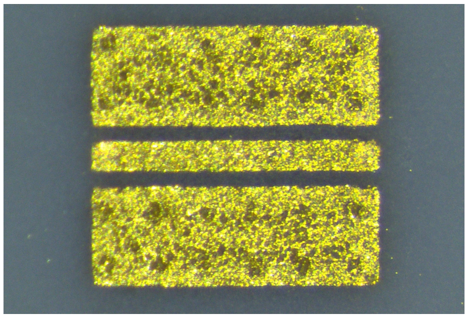

Figure 4.5: CPW transmission lines on LTCC to evaluate signal transmission.

4.2 Design and fabrication of second set structures for the characterization of LTCC material

This section presents the electromagnetic characterization of an LTCC A6M-E substrate combined with thin-film copper metallization. The characterization is performed using resonators and transmission line structures to extract the dielectric constant (ε_r), loss tangent ($\tan\delta$),conductor loss and total loss. Unlike previous studies, this work extends the frequency range up to 180 GHz, covering both the W band and the D band (110–170 GHz), as part of the development of high-frequency components for advanced radio astronomical instrumentation.

In this set test structure, considered two substrate thicknesses (h): 40 μm and 70 μm. The thin-film metallization technology was based on copper deposition, providing a conductor height of 4 µm. A 40nm TiW adhesion layer was added through sputtering deposition.

Microstrip ring resonators (MRR) and transmission lines (TL) were designed following the design method used in [1]. Figure 4.6 show the simulated designs and the fabricated structures of the MRRs and TLs, respectively. These structures were optimized using ANSYS HFSS electromagnetic simulation software to operate in a frequency range from 1 to 180 GHz. Different rings were designed with their dimensions adjusted to achieve resonances centered at 35, 40, 45, 50, and 55 GHz and their harmonic resonances. The TLs were designed with a characteristic impedance of 50 Ω and three different lengths. The dimensions of the TLs were designed to be twice the length of the smaller lines, to allow L2L deembedding [33].

The main geometrical parameters of the structures shown in Fig. 4.6 are denoted as follows: r_m is the mean radius of the MRR, and W_r is the width of the ring trace. For the feed lines of the MRR and the reference TL, W_f represents the line width and L the total line length. In the pad region, L_p and W_p indicate the length and width of the transition pads, respectively. The substrate thickness is denoted as h, and the vertical metallized vias that connect the top metal layer to the bottom ground plane are also illustrated. Table 4.2 summarizes the design dimensions and the obtained fabricated parameters.

4.3 Measurements setup

The laboratory equipment used to perform the S-parameters measurements at W band was the HP-8510C Vector Network Analyzer (VNA), with W-band frequency extenders. For the calibration of the VNA, the HP-8510C equipment is configured in full 2-Port mode, and a standard LRRM calibration is performed based on the use of GGBs CS-5 calibration substrate.

The MRR structures are electrically fed using ground-signal-ground (GSG) RF probes. These structures were measured at room and cryogenic temperatures and over the W-band frequency range of 75 to 110 GHz, using RF probes with 150 μm separation pitch.

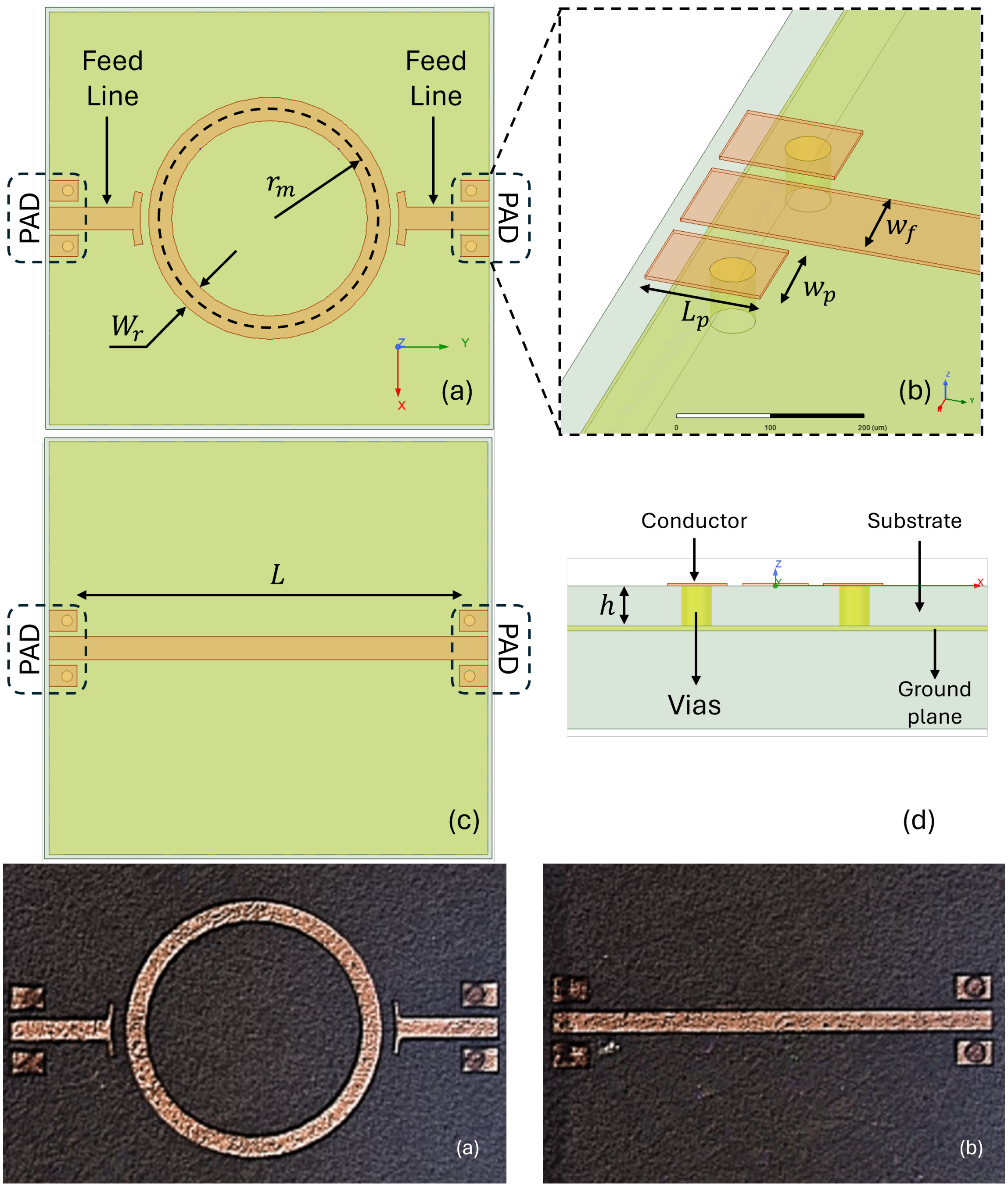

Figure 4.6: Microstrip test structures designed on thin-film LTCC: (a) microstrip ring resonator (MRR), (b) detail of transition pads, (c) microstrip transmission line (TL), (d) side view showing vias and ground plane. Photographs of constructed MRR and TL are shown in (e) and (f), respectively.

Table 4.2: Designed and fabricated dimensions of the MRR and TL structures and their respective transmission pads. Dimensions data are shown for $h = 40$ μm and $h = 70$ μm. Designed line widths were $W_r = 55.5$ μm and $W_r = 108$ μm for substrate heights $h = 40$ μm and $h = 70$ μm, respectively.

MRR Freq.	r_m Design	r_m Fabricated		W_r Fabricated	
		$h = 40$ μm	$h = 70$ μm	$h = 40$ μm	$h = 70$ μm
35 GHz	657	651.0	646.2	30.9	83.3
40 GHz	575	571.0	565.75	30.3	80.9
45 GHz	511	508.5	504.8	30.7	80.9
50 GHz	460	456.65	452.6	30.6	80.9
55 GHz	418	416.5	411.75	34.8	82.0

TL structure	**Length Design [μm]**		**Length Fabricated [μm]**	
	$h = 40$ μm	$h = 70$ μm	$h = 40$ μm	$h = 70$ μm
Short	786.25	894.18	802.5	813.2
Medium	1572.5	1788.37	1596.3	1577
Long	3145	3576.75	3397.2	3126.9

Pad structure	**Length Design [μm]**		**Length Fabricated [μm]**	
	$h = 40$ μm	$h = 70$ μm	$h = 40$ μm	$h = 70$ μm
Wp	124.5	98.25	96.2	100
Lp	172.25	132.25	104.5	144.9
Wf	55.5	108.5	31	84.2

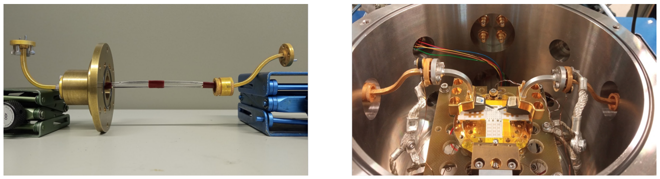
a) b)

Figure 4.7: a) Internal components of the cryogenic chamber with WR-10 waveguide setup for frequencies covering from 75 to 110 GHz, b) View of the location of the cal substrate and the GSG RF probes inside the cryogenic chamber.From: MilliLab - VTT Technical Research Centre of Finland.

A commercial cryogenic probe station was used to perform the tests at ambient temperatures of 300K and 20K. Fig. 4.7 shows the components employed to connect the RF probes, the frequency extenders, and the overall arrangement of all elements used during the measurements inside the cryogenic chamber. The chamber was left open for the measurements at 300K, allowing the temperature to stabilize naturally. In addition, the room temperature measurement was also verified in vacuum with no difference in measurement results. On the other hand, the chamber was hermetically sealed for the measurements at 20K, and the air was evacuated to a high vacuum (HV) before proceeding with the temperature cooling. This setup enables precise and reliable measurements at both temperatures.

5 Results

5.1 S-parameters measurement

5.1.1 First set structure

In Fig. 5.1, 5.2, and 5.3, the forward transmission parameter S_{21} is shown for all measured MRRs within the frequency range from 75 to 110 GHz, and for the rings designed for 80, 90, and 100 GHz, respectively. In these figures, the measurements conducted at room temperature are depicted in red, while those performed under cryogenic and vacuum conditions are shown in blue. The results of the measurements for each MMR are close to each other, which is an indication of the robustness of the fabrication process. Finally, the peak around 107 GHz in the measurements at a temperature of 20 K, which is not present at 300 K, a resonance on the experimental setup waveguide generated during the temperature change cycle. It is relevant to note that this resonance is observed in all the measured MRRs.

The measurements on the CPW transmission line are shown in Fig.5.4. The ambient thermal and vacuum conditions are the same as those used for the measurements of the ring resonators. The results obtained at both temperature conditions show a similar response within the entire frequency band, exhibiting low transmission and return losses (S_{21} and S_{11}, respectively).

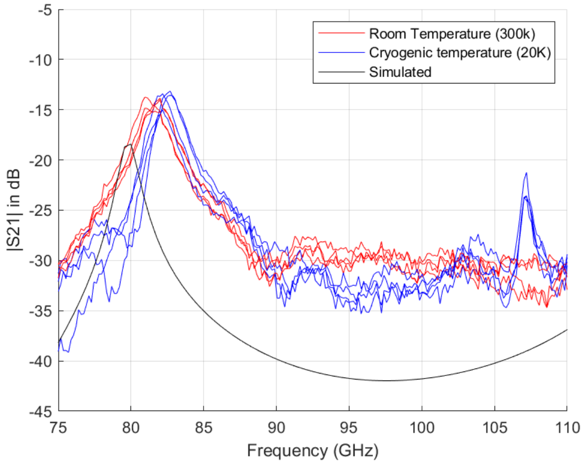

Figure 5.1: Measured and simulated S_{21} for the 80 GHz resonator ring. Red and blue lines correspond to measurements at room and cryogenic temperatures, respectively. Black line corresponds to the microwave simulation of the ring structure [1].

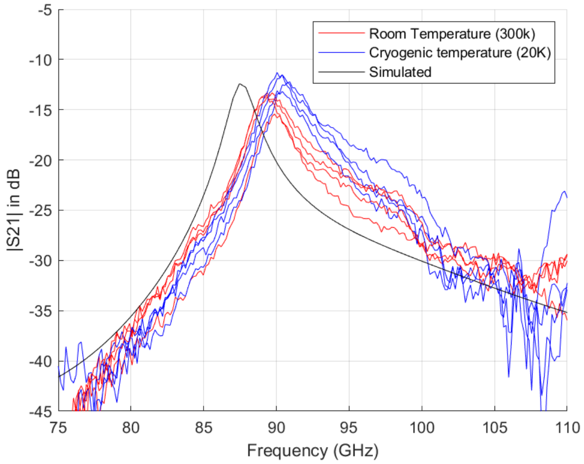

Figure 5.2: Measured and simulated S_{21} for the 90 GHz resonator ring. Color definitions are identical to Fig. 5.1 [1].

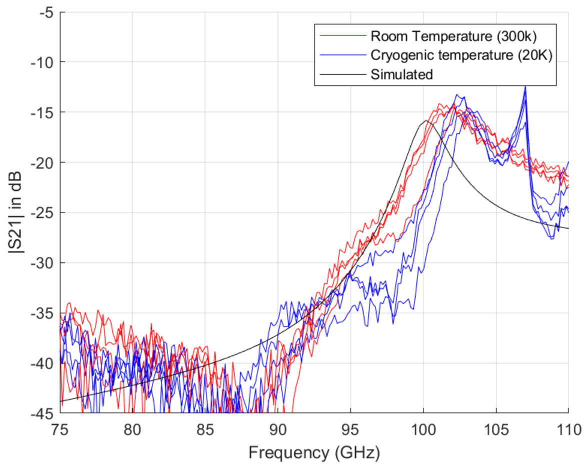

Figure 5.3: Measured and simulated S_{21} for the 100 GHz resonator ring. Color definitions are identical to Fig. 5.1 [1].

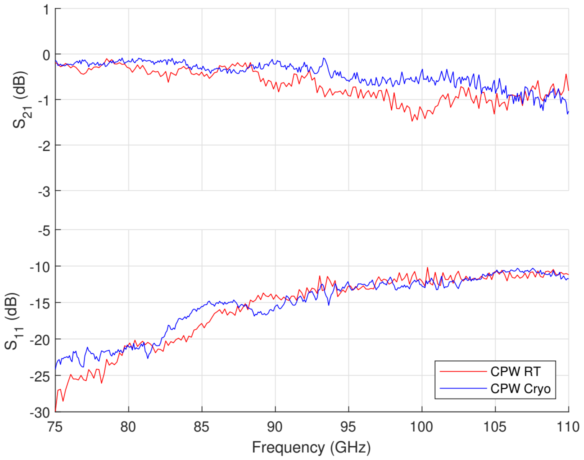

Figure 5.4: Measurement of transmission line CPW scattering parameters with length 1200μ m. Red lines correspond to measurements at room temperature. Blue lines correspond to measurements at cryogenic temperatures [1].

5.1.2 Second set structure

Figure 5.5 compares the simulated and measured transmission coefficients (S_{21}) for the ring resonators. The spectra clearly exhibit fundamental and harmonic resonances, demonstrating good agreement with electromagnetic simulations.

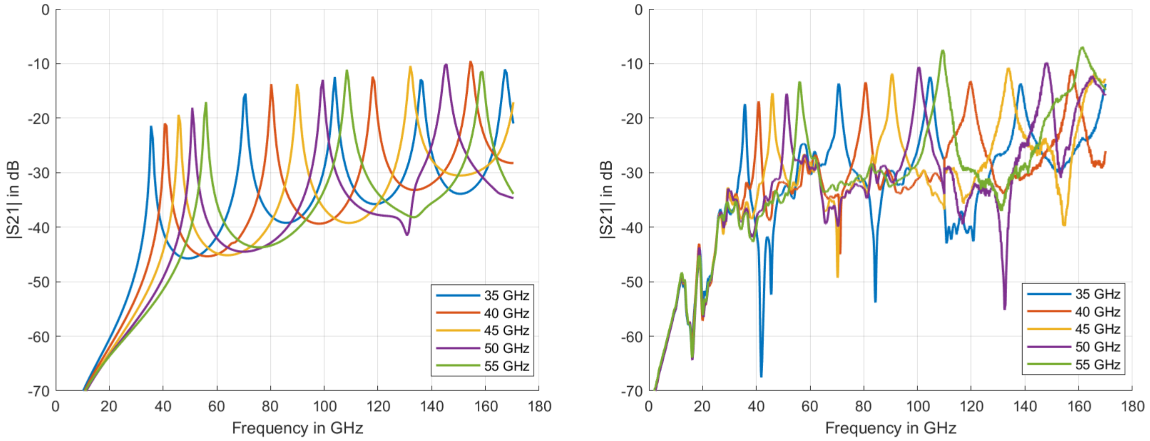

Figure 5.5: Comparison between simulation and measurement results for the designed MRRs. Left: simulated transmission coefficient S_{21} showing fundamental and harmonic resonances up to 180 GHz. Right: measured transmission coefficient S_{21}.

Figures 5.6 and Figures 5.6 show the measured S_{11} and S_{21} for the transmission lines fabricated on substrates with design thicknesses of 40 μm and 70 μm, respectively. Each figure contains three columns corresponding to different transmission line lengths: short, medium, and long (from left to right). For each length, a group of transmission lines was fabricated and measured to evaluate repeatability and consistency.

The S_{21} plots indicate low insertion loss across a broad frequency range, with minimal deviation among lines of the same group. Similarly, the S_{11} curves confirm good impedance matching over a wide bandwidth, particularly in the 40 μm samples, which show slightly better return loss performance compared to their 70 μm coun-

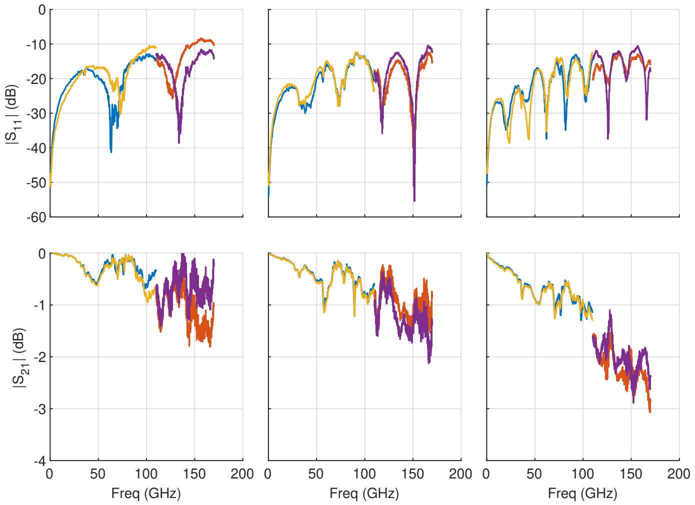

Figure 5.6: Measured transmission and reflection coefficients S_{21} and S_{11} of TLs manufactured with $h = 40$ μm. TL dimensions for short (left), medium (center), and long (right) lines are provided in Table 4.2.

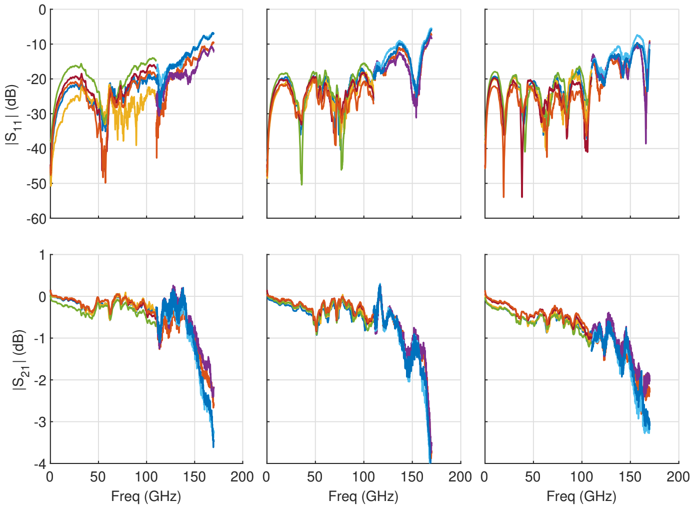

Figure 5.7: Measured transmission and reflection coefficients S_{21} and S_{11} of TLs manufactured with $h = 70$ μm. TL dimensions for short (left), medium (center), and long (right) lines are provided in Table 4.2.

terparts. These results validate the quality of the thin-film metallization process and the effectiveness of the LTCC A6M-E substrate in supporting low-loss propagation up to W- and D-band frequencies.

5.2 Estimation of electrical parameters

To improve the estimation accuracy of the resonant peak frequency (f_r), a Lorentzian function was fitted to the resonance frequency response as suggested in [34], [35]. The fitting procedure was applied to a frequency range close to the resonance peak for both sets of fabricated structures. The results of this Lorentzian fit are the peak frequency and quality factor Q used in the next step to estimate the relative permittivity and loss tangent in the LTCC substrate.

Fig. 5.8 shows the fitting curves at room temperature and cryogenic conditions, respectively. The measured values of the scattering parameters are represented in red and blue for room temperature and cryogenic ambient temperatures, respectively, while the curve obtained from the Lorentzian fit is shown in black.

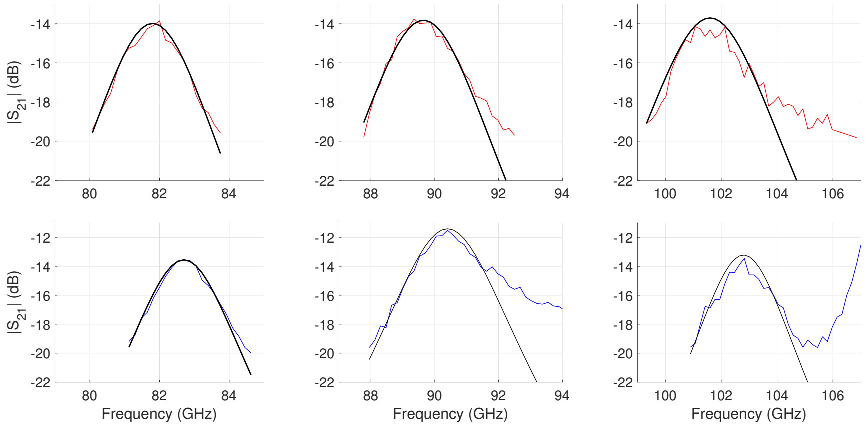

Figure 5.8: Samples of the Lorentzian fits around the resonant peak for measured rings at 80, 90, and 100 GHz, respectively. Red traces are for room temperature measurements, and blue traces are for cryogenic 20 K ambient temperatures [1].

5.2.1 Extraction of the relative dielectric constant

First set MRR structure

The following equations were used to calculate the relative dielectric constant from the derived Lorentzian fits. In our particular single-resonant frequency design $n = 1$, h is the height of the layer (82 μm), and t is the thickness of the conductor 8 μm:

$$\varepsilon_{eff} = \left(\frac{n\, c}{2\, \pi\, r_m\, f_n} \right)^2 \tag{5.1}$$

$$W_{eff} = W + \frac{1.25\, t}{\pi} \left[1 + ln \left(\frac{2\, h}{t} \right) \right] \tag{5.2}$$

$$\varepsilon_r = \frac{2\, \varepsilon_{eff} + \left(1 + 12\, \frac{h}{W_{eff}} \right)^{-\frac{1}{2}} - 1}{\left(1 + 12\, \frac{h}{W_{eff}} \right)^{-\frac{1}{2}} + 1} \tag{5.3}$$

Fig. 5.9 shows the results of the derived relative dielectric constant for each ring sample. Table 5.1 summarizes the average values obtained from the Lorentzian fits and the relative permittivity derived for each set of designed frequencies. As seen from Fig. 5.9, most of the extracted values for each frequency group of rings are close to the nominal relative permittivity obtained from the manufacturer's datasheet [36], shown in a black dotted line. Nevertheless, this figure shows a thermal dependence on the dielectric constant of the Ferro A6M-E substrate, providing a cryogenic value for ε_r approximately 1.82% lower than the room temperature value.

Table 5.1: Summary of the values obtained for the relative permittivity [1].

		300 K		20 K	
MRR structure		f_r (GHz)	ε_r	f_r (GHz)	ε_r
80 GHz	Mean	81.56	6.13	82.43	6.02
	Std	0.33	0.13	0.30	0.11
90 GHz	Mean	89.65	6.09	90.44	5.98
	Std	0.29	0.04	0.36	0.05
100 GHz	Mean	102.04	6.22	102.91	6.11
	Std	0.54	0.04	0.44	0.03

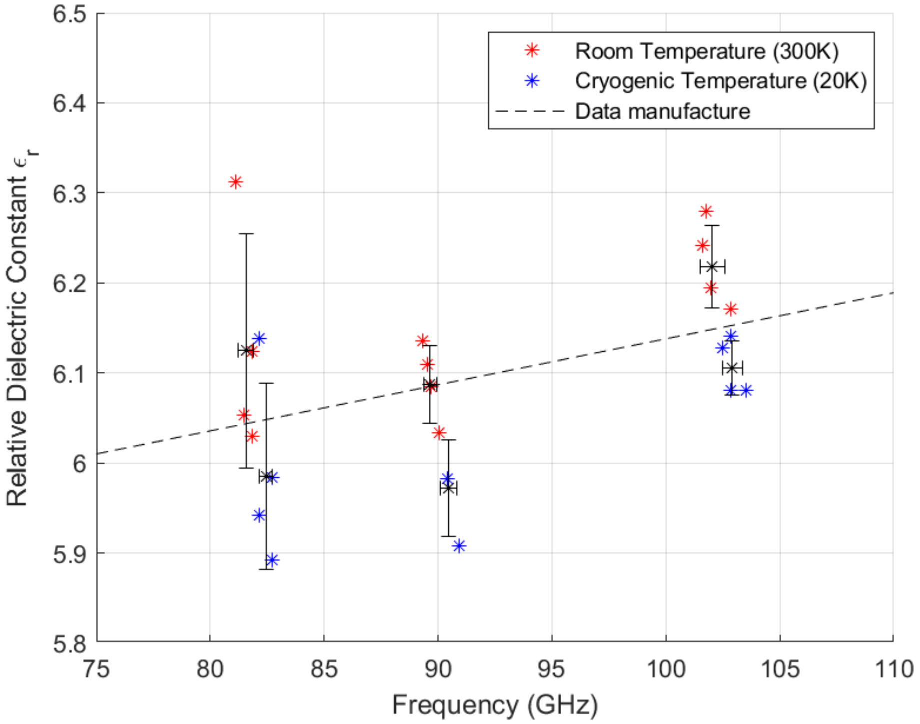

Figure 5.9: Extracted values of relative permittivity ϵ_r of Ferro A6M-E substrate, grouped by design frequency and temperature condition [1].

Second set MRR structure

Similarly, Equations 5.1, 5.2, and 5.3 are applied to this second set of structures. As previously observed in Figure 5.5, the response of the microstrip ring resonators (MRRs) exhibits multiple resonance peaks. In this case, $n = 1, 2, 3, \ldots$, where n denotes the harmonic order and is limited by the highest observable resonance in the measured S-parameter data. The parameter h corresponds to the substrate thickness, and the metallization thickness is fixed at $t = 4\,\mu$m.

Figure 5.10 presents the extracted values of the relative permittivity (ε_r) across the full frequency range from 1 to 180 GHz. The data correspond to four distinct test structures fabricated on LTCC A6M-E substrates: two with a nominal thickness of 40 μm and two with 70 μm. Actual measured thicknesses were 40 μm and 41 μm for the first pair, and 50 μm and 65 μm for the second. Each structure includes multiple resonators, grouped and analyzed as illustrated in the figure. These results provide a detailed characterization of the dielectric behavior of the LTCC A6M-E substrate when used in thin-film integration, confirming its potential suitability for high-frequency applications, including both the W-band and D-band.

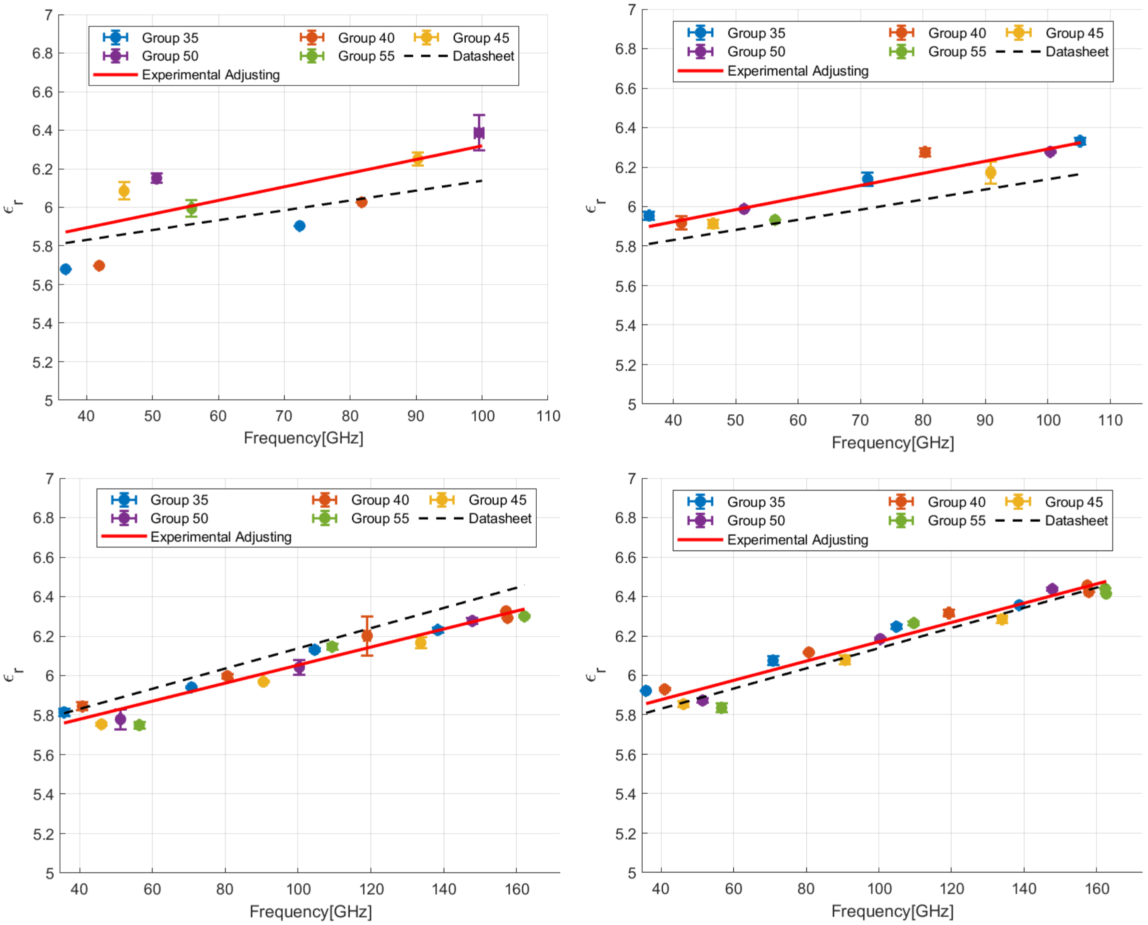

Figure 5.10: Extracted relative permittivity ε_r from different MRRs across four LTCC A6M-E samples with varying substrate thicknesses. The top-left and top-right plots correspond to substrates with measured thicknesses of 40 μm and 41 μm, respectively. The bottom-left and bottom-right plots correspond to thicker substrates with measured values of 50 μm and 65 μm, respectively. Experimental fits are shown in red; the expected response based on measurements of the LTCC manufacturer up to 95 GHz is shown as a dashed black line.

5.2.2 Estimation of Loss Tangent

First set MRR

To extract the loss tangent of the material, a similar methodology to the one previously used for the relative permittivity is exercised. Using the Lorentzian fitting procedure, central frequency and resonance bandwidths are extracted for each group of designed MRRs using equations (5.4) to (5.18). In [37], the equation for determining the tan-δ depends on the dielectric loss, denoted as α_d. The dielectric loss can be extracted from (5.6), where α_{total} represents the attenuation constant of the microstrip resonator, α_c refers to conductor loss, and α_r is the radiation loss.

$$tan\ \delta\left(f_n\right) = \frac{\alpha_d \lambda_0 \sqrt{\varepsilon_{eff}\left(f_n\right)}}{27.3\, \varepsilon_r\left(f_n\right)} \frac{\varepsilon_r\left(f_n\right) - 1}{\varepsilon_{eff}\left(f_n\right) - 1} \tag{5.4}$$

$$\lambda_0 = c/f_n. \tag{5.5}$$

$$\alpha_d = \alpha_{total} - \alpha_c - \alpha_r \tag{5.6}$$

We followed the procedure suggested in [38] to calculate the total loss, as it is required to estimate the dielectric loss. This method is used in substrates that have low losses, as it is the case for LTCC. The method works as follows: the total loss (α_{total}) can be determined at each resonance by computing their loaded quality factor (Q_L) and the unloaded quality factor (Q_u), as detailed in the equations (5.7) and (5.8), and fed by the parameters obtained from the Lorentzian fitting procedure. Results for the estimated α_{total} at both temperatures are shown in Table 5.2. Table 5.3 summarizes the values obtained for both parameters. In (5.7), BW_{3dB}

is the 3 dB bandwidth of the S_{21} resonance peak.

$$Q_L = \frac{f_n}{BW_{3dB}} \tag{5.7}$$

$$Q_u = \frac{Q_L}{1 - 10^{S_{21}(f_n)/20}} \tag{5.8}$$

$$\lambda_g = \frac{c}{\sqrt{\varepsilon_{eff(f_n)}} f_n} \tag{5.9}$$

$$\alpha_{total} = \frac{27.3}{Q_u \lambda_g}, \left[\frac{dB}{m}\right] \tag{5.10}$$

Table 5.2: Results of derived values for α_{total} at both room temperature and cryogenic conditions [1].

		α_{total} (dB/m)	
MRR structure		300 K	20 K
80 GHz	Mean	327.8	255.4
	Std	13.3	14.5
90 GHz	Mean	365.5	286.9
	Std	6.4	5.2
100 GHz	Mean	437.1	311.5
	Std	9.3	11.3

The losses in the conductor (α_c in [dB/m]) must be carefully calculated. The description and analysis of this procedure can be found in the following references: [39], [40], [41], [42]. Equations from (5.11) to (5.17) detail the calculations. In these expressions, Z_{0m} and W_{eff} correspond to the characteristic impedance and effective width of the microstrip [43], [44]. The other necessary parameters are, R_{s1} is the surface-roughness resistance of the conductor, R_s is the surface resistance of the conductor, Δ is the surface roughness (0.6 μm), δ_s skin depth, ρ_c resistivity of the

Table 5.3: Summary of the values obtained for the quality factor Q_L and Q_u [1].

MRR structure		300 K Q_L	300 K Q_u	20 K Q_L	20 K Q_u
80 GHz	Mean	38.09	47.51	48.41	61.07
	Std	1.42	1.79	2.51	3.94
90 GHz	Mean	37.30	46.62	44.07	59.39
	Std	1.52	0.82	1.95	1.11
100 GHz	Mean	35.90	44.84	50.12	62.95
	Std	1.10	1.02	2.43	2.49

conductor for 300 K used $2.249 \times 10^{-8}\Omega$ m and 20 K used $0.0126 \times 10^{-8}\Omega$ m, [45].

$$\alpha_c = \frac{8.68 R_{s1} M}{2\pi Z_{0m} h}\left(1 + \frac{h}{W_{eff}} + \frac{hV}{\pi W_{eff}}\right) \tag{5.11}$$

$$Z_{0m} = \frac{\eta_0}{\sqrt{\varepsilon_{eff}}}\left[\frac{W}{h} + 1.393 + 0.667\, ln\left(\frac{W}{h} + 1.444\right)\right]^{-1} \tag{5.12}$$

$$M = 1 - \left(\frac{W_{eff}}{4h}\right)^2 \tag{5.13}$$

$$V = ln\left(\frac{2h}{t}\right) - \frac{t}{h} \tag{5.14}$$

$$R_{s1} = R_s\left\{1 + \frac{2}{\pi} tan^{-1}\left[1.4\left(\frac{\Delta}{\delta_s}\right)^2\right]\right\} \tag{5.15}$$

$$R_s = \sqrt{\pi\, f\, \mu_0\, \rho_c} \tag{5.16}$$

$$\delta_s = \frac{\rho_c}{R_s} \tag{5.17}$$

To calculate the radiation losses α_r, equations (5.18) and (5.19) from references [46] [47] have been used.

$$\alpha_r = 60\left(\frac{2\pi h}{\lambda_0}\right)^2 F\left(\varepsilon_{eff}\right) \tag{5.18}$$

$$F\left(\varepsilon_{eff}\right) = 1 - \frac{\varepsilon_{eff} - 1}{2\sqrt{\varepsilon_{eff}}} log\left(\frac{\sqrt{\varepsilon_{eff}} + 1}{\sqrt{\varepsilon_{eff}} - 1}\right) \tag{5.19}$$

Finally, the results obtained for the loss tangent for each frequency group of evaluated MRR, are shown in Table 5.4.

Table 5.4: Summary of the results obtained for the loss tangent of Ferro A6M-E substrate at both physical temperatures [1].

		300 K		20 K	
MRR Structure		f_r (GHz)	tan δ 10^{-3}	f_r (GHz)	tan δ 10^{-3}
80 GHz	Mean	81.56	1.78	82.43	1.98
	Std	0.33	0.10	0.30	0.12
90 GHz	Mean	89.65	1.86	90.44	2.04
	Std	0.29	0.05	0.36	0.03
100 GHz	Mean	102.04	2.02	102.91	1.92
	Std	0.54	0.06	0.44	0.07

As it can be seen from the results in Table 5.4, which are shown in detail in Figure 5.11, there is a consistent increase, across frequencies, in the extracted value for the room temperature loss tangent, compared to the data provided by the manufacturer. The overall relative increase is of 16 %. In addition, and focusing on the results obtained at 80 and 90 GHz, there is an overall increase in the loss tangent of about 10 % when the samples are cooled from room temperature to 20 K. The results at 100 GHz did not follow this tendency. We suspect the existence of a waveguide resonant feature that only shows up under cryogenic conditions, and that is spectrally very close to the ring resonance. Such additional resonance would impact the extraction of the quality factor and hence the estimate of the dielectric loss, which is directly proportional to the loss tangent. Although a difference has been obtained in the values of the loss tangent between the two temperature conditions, it does not significantly impact the performance in the W-band, as demonstrated by the response obtained by the CPW line shown in Fig. 5.4.

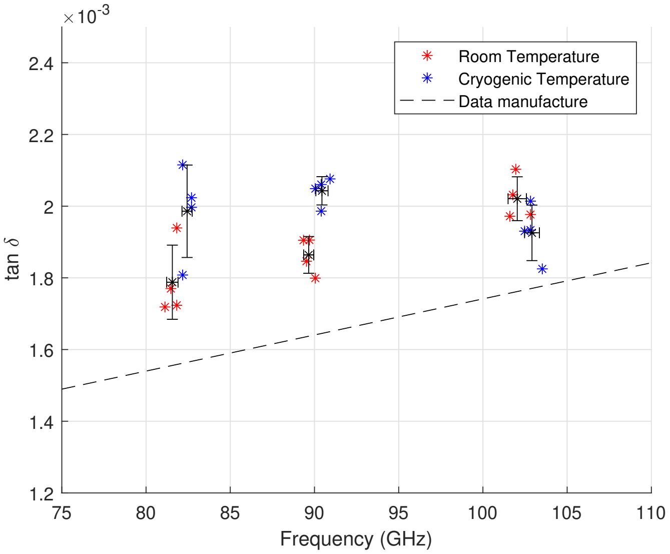

Figure 5.11: Extraction of loss tangent. The results obtained at room temperature are shown as red stars, whereas those obtained under cryogenic conditions (20 K) are shown as blue stars. The dashed line shows the values proposed by the manufacturer[1].

Second set MRR

Following the same procedure used for the first set of microstrip ring resonators (MRRs), the loss tangent ($\tan\delta$) is now calculated for this second set of structures. The calculation is based on Equation 5.4, previously introduced for the initial characterization.

Figure 5.12 shows the extracted values of the loss tangent ($\tan\delta$) as a function of frequency for each group of measured resonators. These results provide insight into the dielectric losses of the LTCC A6M-E substrate across a wide frequency range, with particular focus on the performance of structures using thin-film copper metallization.

The figure includes four subplots corresponding to the same samples presented in Figure 5.10. The top-left and top-right plots show results from the structures fabricated on substrates with measured thicknesses of 40 μm and 41 μm, respectively. The bottom-left and bottom-right plots correspond to substrates with measured thicknesses of 50 μm and 65 μm. Each curve represents the frequency-dependent variation of $\tan\delta$ extracted from multiple resonant peaks. The characterization reveals how the loss behavior evolves with substrate thickness and highlights the consistency and repeatability of the thin-film integration process across different LTCC samples.

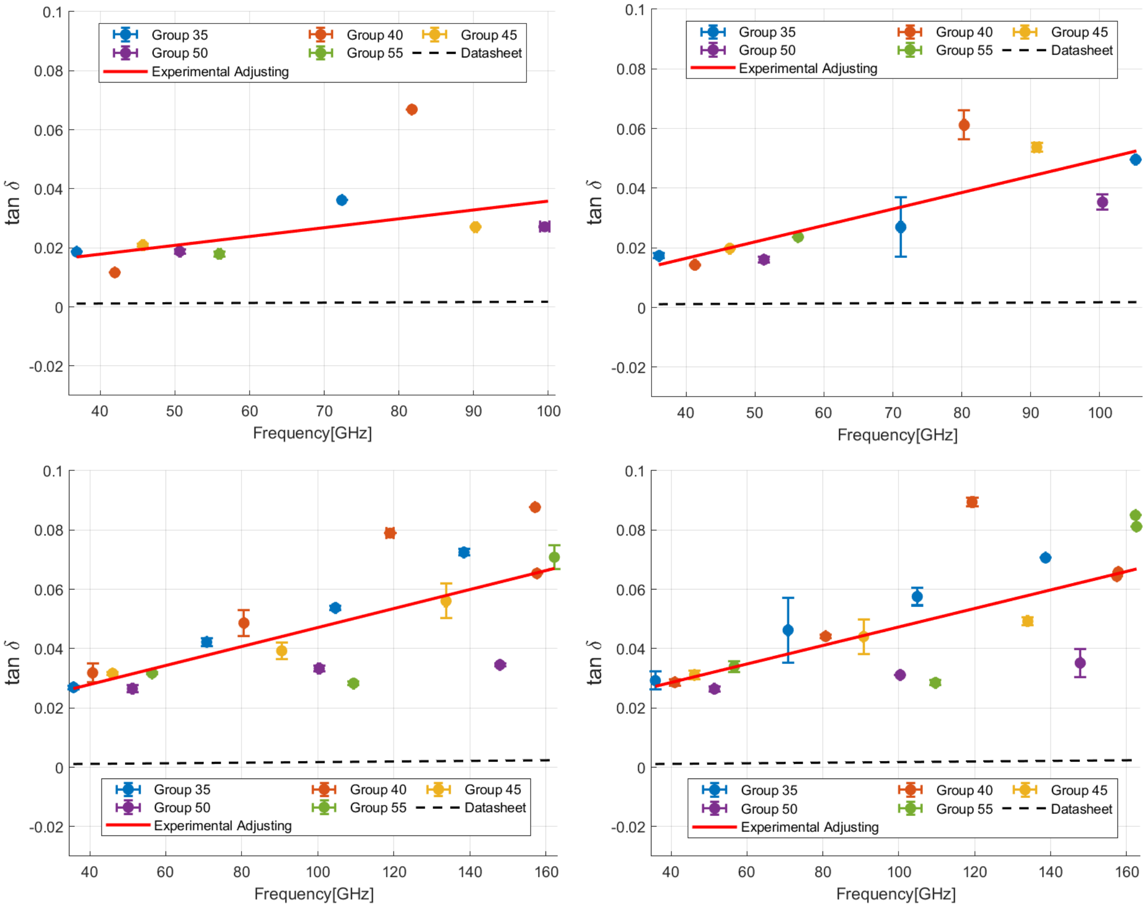

Figure 5.12: Extracted loss tangent ($\tan\delta$) of the same MRR structures of Figure 5.10.

6 Conclusion

The development of this thesis demonstrated the technical feasibility of using the LTCC Ferro A6M-E ceramic substrate at both room and cryogenic temperatures, setting a precedent for the use of this material, particularly in the W band and D band, even when combined with thin-film copper metallization. This opens the path for the next development stage, the integration of high-frequency circuits aimed at radio astronomy instrumentation. Through the experimental methodology presented in this work, the dielectric parameters of the material, specifically, the relative permittivity and the loss tangent, and total loss, were successfully extracted over a wide frequency range from 1 to 180 GHz.

The results obtained show that the material maintains a stable and predictable dielectric behavior under both room-temperature and cryogenically compatible conditions. In particular, the second set of fabricated structures validated the compatibility of this technology with thin-film integration processes, confirming a slightly increasing permittivity profile with frequency.

These results validate the initial hypothesis, confirming that it is possible to develop spectral conversion and amplification modules in the millimeter-wave range through the hybrid integration of InP- and SiGe-based technologies on LTCC substrates. This hybrid approach will not only enable the miniaturization of front-end receiver modules but also offer a solution compatible with multipixel systems for radio astronomy observation.

In this study, we have determined the millimeter-wave electrical properties of LTCC Ferro A6M-E material at room temperature and, for the first time at these wavelengths, under cryogenic conditions. The relative permittivity and loss tangent for this substrate material have been extracted using the microstrip Resonant Ring (MRR) technique at millimeter-waves, on a frequency range of 75 to 110 GHz. We have observed a slight dependence of the derived electrical parameters on the physical temperature of the material. For the relative permittivity, we report an average difference of 1.82% at the two evaluated physical temperatures of 300K and 20K, while the loss tangent showed a difference of 5.3 %.

Based on the results obtained from the second set of structures, the feasibility of integrating thin-film technology with LTCC A6M-E substrates for high-frequency applications is demonstrated. The S-parameters measured from fabricated microstrip ring resonators and transmission lines allowed the extraction of the dielectric constant and loss tangent across a wide frequency range (1–180 GHz). The results confirm that the material exhibits a slightly increasing permittivity with frequency across the band ($\varepsilon_r \approx 5.626 + 5.114 \times 10^{-3} \cdot f\,[\mathrm{GHz}]$) and a low loss tangent ($\tan\delta < 0.1$). These findings position LTCC A6M-E as a competitive candidate for future millimeter-wave system integration.

In conclusion, the electrical properties of the LTCC material have been characterized at the mentioned physical conditions, which is relevant for the use of the material on mm-wave applications that involve cryogenic operations. It should be stated that, to the knowledge of the authors, no previous study has evaluated this substrate in cryogenic conditions at millimeter-wave frequencies. The results demonstrate that a W-band circuit can be designed at room temperature and will only suffer slight differences in cryogenic operations, thus providing a key reference for future uses of the LTCC. Therefore, this study provides essential information for the design of components and sub-systems integrated with this material, and to be used in ultra-sensitive front-end receivers that are aimed for space and astronomy applications.

Future Work

The results presented in this thesis open several promising lines of research that should be explored in future work to consolidate and expand upon the findings obtained.

First, it is essential to perform low-temperature (cryogenic) measurements on LTCC A6M-E structures with thin-film copper metallization. While this thesis addressed the characterization at room temperature, it remains necessary to verify the dielectric behavior under cryogenic conditions. Doing so will allow for a more precise evaluation of the substrate's suitability for highly sensitive millimeter-wave receivers.

Second, the process for extracting the loss tangent ($\tan\delta$) should be refined and extended. A more detailed analysis—potentially involving improved resonator geometries or complementary measurement techniques—will enhance the accuracy and frequency resolution of dielectric loss characterization. This is particularly important for deepening our understanding of how material losses evolve across the W and D bands, and how they correlate with substrate thickness, metallization techniques, and fabrication tolerances.

Finally, based on the dielectric properties confirmed in this study, the development of miniaturized front-end receiver modules using hybrid technology platforms that combine SiGe and InP is now a feasible direction. The electromagnetic behavior demonstrated by the LTCC A6M-E substrate supports its use as an integration platform for these high-performance circuits. Future work should focus on the design and fabrication of fully functional hybrid modules, leveraging InP for ultra-low-noise amplification and SiGe for frequency conversion and signal processing. These modules would directly benefit radio astronomy instrumentation operating in both the W band (75–110 GHz) and the D band (110–170 GHz), contributing to the development of scalable, cryogenically compatible, multi-pixel receiver architectures.

Bibliography

[1] F. Vargas-Millalonco, M. Martínez-Ledesma, R. Reeves, R. Rodríguez, J. Paaso, M. Lahti, M. Kaunisto, and M. Varonen, “Cryogenic characterization of ltcc material in millimeter-wave frequencies,” *IEEE Transactions on Components, Packaging and Manufacturing Technology*, 2024.

[2] E. W. Bryerton, X. Mei, Y.-M. Kim, W. Deal, W. Yoshida, M. Lange, J. Uyeda, M. Morgan, and R. Lai, “A w-band low-noise amplifier with 22k noise temperature,” in *2009 IEEE MTT-S International Microwave Symposium Digest*. IEEE, 2009, pp. 681–684.

[3] R. Davis, A. Wilkinson, R. Davies, W. Winder, N. Roddis, E. Blackhurst, D. Lawson, S. Lowe, C. Baines, M. Butlin *et al.*, “Design, development and verification of the 30 and 44 ghz front-end modules for the planck low frequency instrument,” *Journal of Instrumentation*, vol. 4, no. 12, p. T12002, 2009.

[4] S. Claude, F. Jiang, P. Niranjanan, P. Dindo, D. Erickson, K. Yeung, D. Derdall, D. Duncan, D. Garcia, B. Leckie *et al.*, “Performance of the pre-production band 3 (84-116 ghz) receivers for alma,” in *Millimeter and Submillimeter Detectors and Instrumentation for Astronomy IV*, vol. 7020. International Society for Optics and Photonics, 2008, p. 70201B.

[5] K. Devaraj, S. Church, K. Cleary, D. Frayer, R. Gawande, P. Goldsmith, J. Gundersen, A. Harris, P. Kangaslahti, R. Reeves *et al.*, “Argus: A scalable w-band 16-pixel focal plane array for the green bank telescope,” in *Proc. Interstellar Medium High Redshift Galaxies Comes Age, NRAO Conf. Ser.*, vol. 28, 2012.

[6] M. T. Sebastian, H. Wang, and H. Jantunen, “Low temperature co-fired ceramics with ultra-low sintering temperature: A review,” *Current Opinion in Solid State and Materials Science*, vol. 20, no. 3, pp. 151–170, 2016.

[7] U. Ullah, N. Mahyuddin, Z. Arifin, M. Z. Abdullah, and A. Marzuki, “Antenna in ltcc technologies: a review and the current state of the art,” *IEEE Antennas and Propagation Magazine*, vol. 57, no. 2, pp. 241–260, 2015.

[8] M. Shaik, S. Agarwal, and V. Pabolu, “A miniaturized ltcc rf front-end module for satcom mss handheld terminals,” in *2022 IEEE Wireless Antenna and Microwave Symposium (WAMS).* IEEE, 2022, pp. 1–3.

[9] J. R. Bray, K. T. Kautio, and L. Roy, “Characterization of an experimental ferrite ltcc tape system for microwave and millimeter-wave applications,” *IEEE transactions on advanced packaging*, vol. 27, no. 3, pp. 558–565, 2004.

[10] Y.-s. Dai, H.-h. Yin, H.-t. Sun, Y. Feng, Q.-y. Xie, and M. Luo, “A miniaturized millimeter-wave bandpass filter with ltcc technology,” in *2012 IEEE MTT-S International Microwave Workshop Series on Millimeter Wave Wireless Technology and Applications.* IEEE, 2012, pp. 1–3.

[11] Y. Zhang, X. Tang, X. Wu, J. Chen, Y. Jing, and H. Su, “Effect of bi2o3 and co2o3 co-doping on power loss characteristics of low-temperature-fired nicuzn

ferrites," *Journal of Magnetism and Magnetic Materials*, vol. 555, p. 169368, 2022.

[12] H. Jantunen, T. Kangasvieri, J. Vähäkangas, and S. Leppävuori, "Design aspects of microwave components with ltcc technique," *Journal of the European Ceramic Society*, vol. 23, no. 14, pp. 2541–2548, 2003.

[13] M. V. Jacob, J. Mazierska, and M. Bialkowski, "Measurement of complex permittivity of low temperature co-fired ceramic at cryogenic temperatures," *Advances in Electronic Ceramic Materials: Ceramic Engineering and Science Proceedings*, vol. 26, pp. 209–216, 2005.

[14] E. Bryerton, M. Morgan, and M. W. Pospieszalski, "Ultra low noise cryogenic amplifiers for radio astronomy," in *2013 IEEE Radio and Wireless Symposium*. IEEE, 2013, pp. 358–360.

[15] W. Ramírez, H. Forstén, M. Varonen, R. Reeves, M. Kantanen, K. Mehmet, and S. Torres, "Cryogenic operation of a millimeter-wave sige bicmos low-noise amplifier," *IEEE Microwave and Wireless Components Letters*, vol. 29, no. 6, pp. 403–405, 2019.

[16] M. Varonen, N. Sheikhipoor, B. Gabritchidze, K. Cleary, H. Forstén, H. Rücker, and M. Kaynak, "Cryogenic w-band sige bicmos low-noise amplifier," in *2020 IEEE/MTT-S International Microwave Symposium (IMS)*. IEEE, 2020, pp. 185–188.

[17] A. Lamminen, "Design of millimetre-wave antennas on low temperature co-fired ceramic substrates: Master's thesis," 2006.

[18] M. T. Sebastian, R. Ubic, and H. Jantunen, *Microwave materials and applications.* John Wiley & Sons, 2017.

[19] R. Kulke, M. Rittweger, P. Uhlig, and C. Günner, "Ltcc-multilayer ceramic for wireless and sensor applications," *IMST GmbH, http://www. ltcc. de*, 2001.

[20] M. Lahti, K. Kautio, M. Karppinen, K. Keränen, J. Ollila, and P. Karioja, "Review of ltcc technology for millimeter waves and photonics," *International Journal of Electronics and Telecommunications*, vol. 66, 2020.

[21] D. M. Pozar, "Microwave engineering," *Fourth Editions, University of Massachusetts at Amherst, John Wiley & Sons, Inc*, pp. 26–30, 2012.

[22] I. Elfergani, A. S. Hussaini, A. M. Abdalla, J. Rodriguez, and R. Abd-Alhameed, "Millimeter wave antenna design for 5g applications," *Optical and Wireless Convergence for 5G Networks*, pp. 139–156, 2019.

[23] A. R. Fulford and S. M. Wentworth, "Conductor and dielectric-property extraction using microstrip tee resonators," *Microwave and Optical Technology Letters*, vol. 47, no. 1, pp. 14–16, 2005.

[24] J. Baker-Jarvis, M. Janezic, B. Riddle, R. Johnk, C. Holloway, R. Geyer, and C. Grosvenor, "Nist technical note 1536," *Measuring the Permittivity and Permeability of Lossy Materials: Solids, Liquids, Metals, Building Materials, and Negative-Index Materials*, 2005.

[25] Y. Balega, O. Bolshakov, A. Chernikov, A. Gunbina, V. Edelman, M. Efimova, A. Eliseev, A. Krasilnikov, I. Lapkin, I. Lesnov, M. Mansfeld, M. Markina, E. Pevzner, S. Shitov, A. Smirnov, M. Tarasov, N. Tyatushkin, A. Vdovin, and V. Vdovin, "Development of cryogenic systems for

astronomical research," *Photonics*, vol. 11, no. 3, 2024. [Online]. Available: https://www.mdpi.com/2304-6732/11/3/257

[26] M. Božanić and S. Sinha, "Emerging transistor technologies capable of terahertz amplification: A way to re-engineer terahertz radar sensors," *Sensors*, vol. 19, no. 11, p. 2454, 2019.

[27] M. Varonen, R. Reeves, P. Kangaslahti, L. Samoska, J. W. Kooi, K. Cleary, R. S. Gawande, A. Akgiray, A. Fung, T. Gaier *et al.*, "An mmic low-noise amplifier design technique," *IEEE Transactions on Microwave Theory and Techniques*, vol. 64, no. 3, pp. 826–835, 2016.

[28] J. D. Preez, S. Sinha, and K. Sengupta, "Sige and cmos technology for state-of-the-art millimeter-wave transceivers," *IEEE Access*, vol. 11, pp. 55 596–55 617, 2023.

[29] I. Song, G. Ryu, S. H. Jung, J. D. Cressler, and M.-K. Cho, "Wideband sige-hbt low-noise amplifier with resistive feedback and shunt peaking," *Sensors*, vol. 23, no. 15, p. 6745, 2023.

[30] K. H. Yau, P. Chevalier, A. Chantre, and S. P. Voinigescu, "Characterization of the noise parameters of sige hbts in the 70–170-ghz range," *IEEE Transactions on Microwave Theory and Techniques*, vol. 59, no. 8, pp. 1983–2000, 2011.

[31] T. Yu and D. Yu, "Electrical performance characterization of glass substrate for millimeter-wave applications," *Journal of Materials Science: Materials in Electronics*, vol. 34, no. 2, p. 126, 2023.

[32] M. Kirschning and R. H. Jansen, “Accurate model for effective dielectric constant of microstrip with validity up to millimetre-wave frequencies,” *Electronics letters*, vol. 6, no. 18, pp. 272–273, 1982.

[33] J. C. Rautio, “A de-embedding algorithm for electromagnetics,” *International Journal of Microwave and Millimeter-Wave Computer-Aided Engineering*, vol. 1, no. 3, pp. 282–287, 1991. [Online]. Available: https://onlinelibrary.wiley.com/doi/abs/10.1002/mmce.4570010306

[34] L.-F. Chen, C. K. Ong, C. Neo, V. V. Varadan, and V. K. Varadan, *Microwave electronics: measurement and materials characterization.* John Wiley & Sons, 2004.

[35] G. Gugliandolo, G. Vermiglio, G. Cutroneo, G. Campobello, G. Crupi, and N. Donato, “Development, characterization, and circuit modeling of inkjet printed coupled ring resonators for application in biological samples,” *IEEE Transactions on Instrumentation and Measurement*, 2023.

[36] “Ferro a6m datasheet,” Dec 2023. [Online]. Available: https://www.etsmtl.ca/Unites-de-recherche/LTCC/Services-offerts/Ferro_A6M.pdf

[37] M. Schneider, B. Glance, and W. Bodtmann, “Microwave and millimeter wave hybrid integrated circuits for radio systems,” *Bell System Technical Journal*, vol. 48, no. 6, pp. 1703–1726, 1969.

[38] G. K C, “Microstrip lines and slotlines,” 1996.

[39] R. A. Pucel, D. J. Masse, and C. P. Hartwig, “Losses in microstrip,” *IEEE transactions on microwave theory and techniques*, vol. 16, no. 6, pp. 342–350, 1968.

[40] K. Chang and L.-H. Hsieh, *Microwave ring circuits and related structures.* John Wiley & Sons, 2004, vol. 156.

[41] N. Aslani-Amoli, M. ur Rehman, F. Liu, M. Swaminathan, C.-G. Zhuang, N. Z. Zhelev, S.-H. Seok, and C. Kim, "Characterization of alumina ribbon ceramic substrates for 5g and mm-wave applications," *IEEE Transactions on Components, Packaging and Manufacturing Technology*, vol. 12, no. 9, pp. 1432–1445, 2022.

[42] R. Garg, I. Bahl, and M. Bozzi, *Microstrip lines and slotlines.* Artech house, 2013.

[43] L.-l. Yang, L. Sun, Q. Shi, and H.-y. Sun, "Extraction of dielectric constant based on s-parameter inversion method," in *2011 3rd International Conference on Computer Research and Development*, vol. 3. IEEE, 2011, pp. 353–356.

[44] E. O. Hammerstad, "Equations for microstrip circuit design," in *1975 5th European Microwave conference.* IEEE, 1975, pp. 268–272.

[45] R. A. Matula, "Electrical resistivity of copper, gold, palladium, and silver," *Journal of Physical and Chemical Reference Data*, vol. 8, no. 4, pp. 1147–1298, 1979.

[46] B. C. Wadell, "Transmission line design handbook," *(No Title)*, 1991.

[47] N. Mahjabeen, J. Bright, S. R. Aroor, N. Virushabadoss, S. Surendar, K. S. Elassy, W. A. Shiroma, A. T. Ohta, and R. Henderson, "Low-cost rapid prototyping of ring resonator for dielectric characterization of packaging substrates," in *2020 IEEE Texas Symposium on Wireless and Microwave Circuits and Systems (WMCS).* IEEE, 2020, pp. 1–4.